Implied Ocean Heat Transports in the Standard and Superparameterized Community Atmospheric Models

CHARLOTTE A. DEMOTT AND DAVID A. RANDALL

Department of Atmospheric Science, Colorado State University, Fort Collins, Colorado

MARAT KHAIROUTDINOV

School of Marine and Atmospheric Sciences, Stony Brook University, Stony Brook, New York

(Manuscript received 16 December 2008, in final form 23 July 2009)

ABSTRACT

Implied ocean heat transport (T_o) based on net surface energy budgets is computed for two versions of the Community Atmospheric Model (CAM, version 3.0) general circulation model (GCM). The first version is the standard CAM with parameterized convection. The second is the multiscale modeling framework (MMF), in which parameterized convection is replaced with a two-dimensional cloud-resolving model in each GCM grid column. Although global-mean net surface energy totals are similar for both models, differences in the geographic distributions of the component errors lead to distinctly different T_o for each model, with CAM's T_o generally agreeing with observationally based T_o estimates, and the MMF's T_o producing northward transport at all latitudes north of ~50°S.

Analysis of component error sources in the T_o calculation identifies needed improvements in the MMF. Net surface shortwave radiation and latent heat fluxes over the oceans are the primary causes of T_o errors in the MMF. Surface shortwave radiation biases in the MMF are associated with liquid and/or ice water content biases in tropical and extratropical convection and a deficit of marine stratocumulus clouds. It is expected that tropical ice water contents in the MMF can be made more realistic via improvements to the cloud microphysics parameterization. MMF marine stratocumulus clouds are overly sensitive to low-level relative humidity and form only with nearly saturated conditions and a shallow boundary layer. Latent heat flux errors in the MMF are amplifications of those found in the CAM and are concentrated in the trade wind regime and the Asian monsoon region and the adjacent western Pacific Ocean.

Potential improvements to T_o are estimated by replacing either simulated net surface shortwave or latent heat fluxes with those from observations and recomputing T_o. When observed shortwave fluxes are used, both CAM and MMF produce greatly improved T_o curves for both hemispheres. When T_o is computed using observed latent heat fluxes, CAM T_o degrades slightly and MMF T_o improves, especially in the sign of Southern Hemisphere transport.

1. Introduction

Circulation of the earth's atmosphere and oceans results from the disparity between net radiation receipts in low latitudes and net radiation loss at the poles. Planetary rotation, the division of the earth's surface into solid and liquid spheres, and the presence of atmospheric water vapor and polar ice caps result in a complex joint ocean–atmosphere circulation system in which both the ocean and atmosphere redistribute the net incoming tropical energy.

Estimating the total required meridional energy transport and the contributions by the atmosphere and ocean began with Houghton (1954), who computed estimates of the total required transport by extrapolating North American surface radiation measurements about the globe, adjusting for globally varying surface properties and cloud fractions, and then calculating the net radiation balance at the top of the atmosphere (TOA). Oceanic heat transports were computed from surface energy budget studies (Sverdrup 1957) and in situ hydrographic data (Jung 1952; Bryan 1962), while atmospheric transports were estimated based on sounding data (Oort 1971).

Corresponding author address: Charlotte DeMott, Department of Atmospheric Science, Colorado State University, Fort Collins, CO 80523.
E-mail: demott@atmos.colostate.edu

DOI: 10.1175/2009JCLI2987.1

© 2010 American Meteorological Society

These early studies demonstrate creative solutions to a well-understood problem but suffered from a lack of physical constraints on the solution. By the 1970s, several years of satellite data provided the needed upper boundary condition (top-of-atmosphere net radiation), which yielded a direct estimate of total required transport. Vonder Haar and Oort (1973) examined the Northern Hemisphere total required transport computed from satellite data and the atmospheric transport computed from sounding data to calculate ocean transport as a residual, while Trenberth (1979) performed a similar analysis for the Southern Hemisphere. These results and other studies (e.g., Hasternath 1980; Carissimo et al. 1985) revealed oceanic transports significantly greater than initially estimated.

Estimates of the atmosphere–ocean partition of meridional energy transport have been further refined with the availability of global atmospheric reanalysis datasets and an expanding array of oceanic transport point measurements. Reanalysis products allow implied ocean heat transport to be calculated either as a residual of the TOA-derived required transport (computed from satellite observations) minus the atmospheric vertically integrated total energy meridional transport (which mimics the sounding data approach) or, more directly, from the analyzed net surface energy budget over the oceans. For the latter approach, net sensible and latent heat fluxes are heavily influenced by the formulation of the assimilating model. Trenberth and Caron (2001) derived oceanic transports computed from the National Centers for Environmental Prediction (NCEP) and European Centre for Medium-Range Weather Forecasts (ECMWF) reanalysis products using the residual method, and Trenberth et al. (2001) compared the results to transports computed from reanalysis model-derived surface heat fluxes. Their results highlight a number of shortcomings in both the input data and the assimilation system that affect both calculations but suggest that the residual method of computing ocean heat transport is less prone to model biases than the surface flux method. Importantly, residual-derived ocean heat transports show reasonable agreement with in situ oceanic measurements (see also Trenberth and Fasullo 2008).

While observationally based estimates of atmospheric and oceanic transports are subject to uncertainties, they are sufficiently well-known to serve as a basis for model evaluation and can serve as a useful ''reality check'' on the fidelity of atmospheric global circulation models (AGCMs). Gleckler et al. (1995) analyzed implied oceanic transports from the net surface energy fluxes simulated by 15 AGCMs participating in the Atmospheric Model Intercomparison Project (AMIP; Gates 1992) and found little agreement with observations, with many models yielding northward oceanic transport for both Northern and Southern Hemispheres. Further analysis revealed that cloud radiative effects were the leading cause of error in the oceanic transport, or T_o, calculation. Replacing simulated TOA radiation with observed radiation resulted in more realistic T_o values, suggesting that model improvements to cloud radiative effects are the most direct path to improved T_o simulations. Hack (1998) examined Community Climate Model (CCM, version 3) T_o calculated from the surface energy budget and found that surface latent heat flux errors also played a critical role in simulating T_o. These studies demonstrate that analysis of T_o from AGCMs can serve as a focusing mechanism to reveal biases in model formulation which result in unrealistic large-scale circulation features. For AGCMs that will be coupled to ocean models, correctly simulating the surface energy budget, and the implied ocean heat transport is necessary to achieve realistic coupled simulations and to avoid climate drift in the coupled system.

In this study, we employ the concept of implied ocean heat transport as a diagnostic tool. This approach is attractive because T_o provides a globally integrated estimate of model biases, and those biases can be traced back to model shortcomings particular to geographic location, seasonal variations, or even specific physical process. We apply this approach to two configurations of the Community Atmospheric Model, version 3.0 (CAM3; Collins et al. 2006). The first configuration is the ''standard'' CAM available from the Community Climate System Model (CCSM) Web site. The second is the recently developed ''multiscale modeling framework'' (MMF; Khairoutdinov and Randall 2001), in which the cumulus parameterizations of CAM3 are replaced with a two-dimensional cloud-resolving model (CRM) at each GCM grid column.

The MMF is a considerable departure from traditional parameterizations, so our first goal is to simply assess how it affects T_o in the CAM. Although the MMF has improved some aspects of the simulated climate in the CAM (notably the diurnal cycle of precipitation and tropical variability; Khairoutdinov and Randall 2003; Khairoutdinov et al. 2005), it has also introduced new biases, such as increased ice water in tropical clouds compared to CAM, anomalously high boreal summer northwestern Pacific precipitation, and a low frequency of marine stratocumulus clouds. Until now, the net effects and degree of importance of these various improvements and biases for T_o have not been known. The second goal of our study, therefore, is to evaluate the individual components of T_o and compare the MMF results to those from the standard CAM and to observations. Ultimately, such an analysis should highlight

TABLE 1. Net global-mean TOA and surface (sfc) energy fluxes and precipitation for CAM and MMF AMIP-type simulations.

	Net TOA ($W\ m^{-2}$)	Net sfc ($W\ m^{-2}$)	TOA − sfc ($W\ m^{-2}$)	(TOA − sfc)/Net TOA (%)	$E - P$ ($W\ m^{-2}$)	$(E - P)/E$ (%)	R ($mm\ day^{-1}$)
CAM	3.19	0.66	2.53	1.1	0.06	0.1	2.83
MMF	0.53	−1.37	1.90	0.8	0.07	0.1	2.80

biases in physical processes, either global or regional, which, when corrected, would have the greatest impact on improving T_o.

Our paper is arranged as follows: section 2 provides a brief description of the standard CAM and MMF. The T_o computations and an analysis of surface energy budget components are presented in section 3. Section 4 contains a discussion of the leading sources of error in the MMF's simulated T_o, and section 5 summarizes the work.

2. Model description and comparison datasets

This work utilizes model output from two configurations of the CAM3 (Collins et al. 2006). The first is the CAM in its standard configuration as distributed via the CCSM Web site (http://www.ccsm.ucar.edu/), which utilizes the deep and shallow cumulus parameterizations of Zhang and McFarlane (1995) and Hack et al. (1993), respectively. We run the model using the semi-Lagrangian dynamical core (Williamson and Olson 1994), which was chosen for its scalability when running on multiple computer processors. In the second model, the MMF, convective tendencies are computed with the System for Atmospheric Modeling (SAM; Khairoutdinov and Randall 2003) cloud-resolving model, which is run instead of the parameterizations in the CAM3. Each model was run in AMIP mode, using observed sea surface temperatures (Reynolds et al. 2007) as the lower boundary condition, for the years 1986–99.

It is important to note that the CAM has been tuned over the years to produce a near-zero TOA net radiation imbalance (mean of ~0.1 $W\ m^{-2}$ for the spectral dynamical core; mean of ~3 $W\ m^{-2}$ for our control run) and reasonable cloud properties. Such tuning, which is typically performed via cloud microphysical adjustments, is necessary to avoid spurious climate drift in long-term simulations. In contrast, the MMF is still an evolving modeling framework and has only been minimally tuned to produce a near-zero TOA net radiation imbalance (−0.53 $W\ m^{-2}$ for this run). Additional details concerning the energy balance in the CAM and MMF are provided in Table 1. TOA and surface energy imbalances result in a net energy gain to both CAM and MMF atmospheres on the order of ~1% of net incoming radiation per year. Global-mean precipitation and evaporation minus precipitation ($E - P$) differ by 1% or less for the two models. Global-mean rainfall exceeds the Climate Prediction Center (CPC) Merged Analysis of Precipitation (CMAP; Xie and Arkin 1997) estimate of 2.69 $mm\ day^{-1}$ by 5% for CAM and 4% for MMF. Although the close agreement between CAM and MMF energy balance figures is somewhat fortuitous, the results of Table 1 provide confidence that model differences do not result from gross differences in the net energy balance. As we shall see, however, the near-zero TOA net radiation balance in the MMF is achieved despite remaining biases in cloud properties. Finally, it should be noted that CAM results with the semi-Lagrangian dynamical core differ from the version based on the spectral dynamical core, and implied ocean heat transports with that dynamical core exhibit slightly better agreement with observations than the semi-Lagrangian results.

An expanded description of the two model configurations is given in DeMott et al. (2007) and is not repeated here, except to summarize the previously identified major differences between the CAM and MMF: compared to the CAM, the MMF 1) improves the diurnal cycle of nondrizzle precipitation over land, 2) produces a more realistic distribution of cirrus clouds, 3) improves the spectrum of tropical weather variability, 4) introduces a negative bias in marine stratocumulus cloud amount, and 5) is characterized by a large positive precipitation bias in the northwest Pacific Ocean during boreal summer.

Implied ocean heat transports, computed from the 14-yr mean surface energy budget, are compared to T_o results of Trenberth and Caron (2001), which are computed using TOA net radiation measurements from the Earth Radiation Budget Experiment (ERBE; Barkstrom and Hall 1982) and atmospheric transports from National Centers for Environmental Prediction (NCEP; Kistler et al. 2001) reanalysis and the 40-yr ECMWF Re-Analysis (ERA-40; Uppala et al. 2005). Additional datasets used for comparison of surface energy budget components are discussed in the following sections.

3. The T_o from net surface energy budgets

Computation of T_o from AGCMs is most simply obtained by integrating the oceanic zonally integrated annual mean net surface energy flux over all latitudes. To ensure zero transport at the poles, the area-weighted

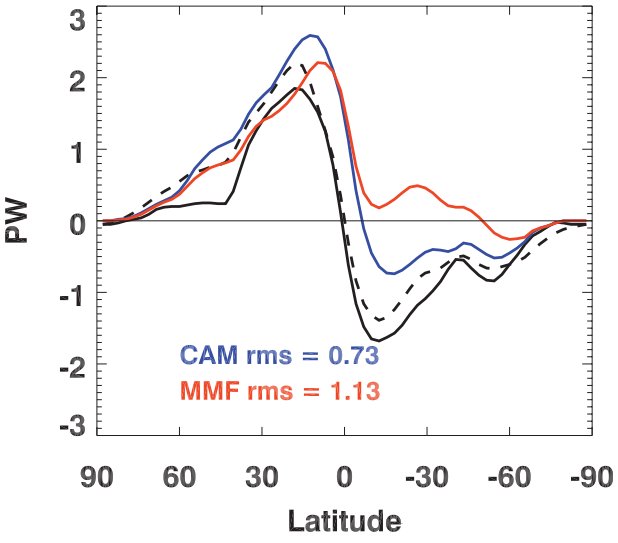

FIG. 1. Implied ocean heat transports as a function of latitude (in units of petawatts). CAM is shown in blue, MMF is shown in red, and the NCEP (solid) and ERA-40 (dashed) estimates of Trenberth and Caron (2001) are shown for comparison.

mean net oceanic surface heat flux (11.0 W m^{-2} for CAM; 10.6 W m^{-2} for the MMF) is subtracted from all ocean points. The implied ocean heat transport T_o imposed by the atmosphere as a function of latitude is then given by

$$T_o(\phi) = 2\pi a^2 \int_{-\pi/2}^{\phi} N_o \cos\phi' \, d\phi', \qquad (1)$$

where j is latitude, a is the earth's radius, and N_o is the zonally integrated net surface energy flux over the ocean, N_o = netSW − netLW − LH − SH, defined as the sum of net surface shortwave (netSW) and longwave (netLW) radiation, and latent and sensible heat fluxes (LH and SH, respectively).

Implied ocean heat transports for the CAM and MMF are shown in Fig. 1, with comparison curves from Trenberth and Caron (2001) based on ERBE TOA radiation data and NCEP and ERA-40 atmospheric data. The NCEP and ERA-40 T_o curves are not computed from NCEP and ERA-40 surface flux variables. While these quantities are readily available at all points on the globe from AGCMs, reliable observational estimates of surface fluxes are hampered by inadequate observing systems. Instead, the NCEP and ERA-40 curves are obtained via the residual method described in Trenberth and Caron (2001), which results in better agreement with point estimates of oceanic transport. Although the CAM generally produces the correct shape of T_o, there is too much poleward transport in the Northern Hemisphere and too little in the Southern Hemisphere. The MMF, on the other hand, produces northward transport for all latitudes north of ~50°S. The lack of MMF poleward transport in the Southern Hemisphere is typical of untuned or minimally tuned AGCMs, as shown by Gleckler et al. (1995).

In the following subsection, we explore sources of error in T_o. The goal of this analysis is to illuminate problems in each model that, when corrected, should lead to improved T_o estimates. In the case of the MMF, we also wish to learn how the "superparameterization" changes the simulation.

The T_o *errors: Zonal-mean depictions*

Oceanic zonal-mean values of annual-mean net surface shortwave (SW) and longwave (LW) radiation and LH and SH and their biases compared to observations are shown in Fig. 2. Comparison of the top panels (Figs. 2a–d) illustrates the dominance of shortwave radiation and latent heat fluxes on the net surface energy budget, especially in the low latitudes. Near the poles, longwave radiation and sensible heat fluxes are comparable to shortwave radiative and latent heat fluxes.

Surface energy fluxes are compared to their respective observational "best estimates" in Figs. 2e–h. Latent and sensible heat fluxes are compared to the newly available 50-yr objectively analyzed air–sea flux (OAFlux) project (Yu and Weller 2007). The OAFlux dataset combines satellite and reanalysis products, which incorporate in situ observations of surface variables. OAFlux data are distributed with shortwave and longwave radiation flux observations from the International Satellite Cloud Climatology Project (ISCCP) dataset (Zhang et al. 2004), which are used to compare simulated SW and LW fields. ISCCP SW and LW global error estimates are conservatively estimated by Zhang et al. (2004) to be 10–15 W m^{-2}, which is comparable to the largest reported errors in the OAFlux LH and SH estimates (Yu and Weller 2007).

CAM and MMF net surface SW and LW flux errors are similar, and largest at the poles, although the MMF receives less surface insolation near the equator and more LW at the poles. Because the radiation code is the same for CAM and MMF, these differences must arise from differences in cloud properties or water vapor. Khairoutdinov et al. (2005) have speculated that increased tropical ice water content in the MMF may be the cause of tropical MMF shortwave radiation errors. The greatest model-to-observation differences are seen in the subtropical latent heat fluxes, with MMF errors nearly double those of the CAM. Sensible heat flux errors are small for both models, except in the Southern Hemisphere high latitudes.

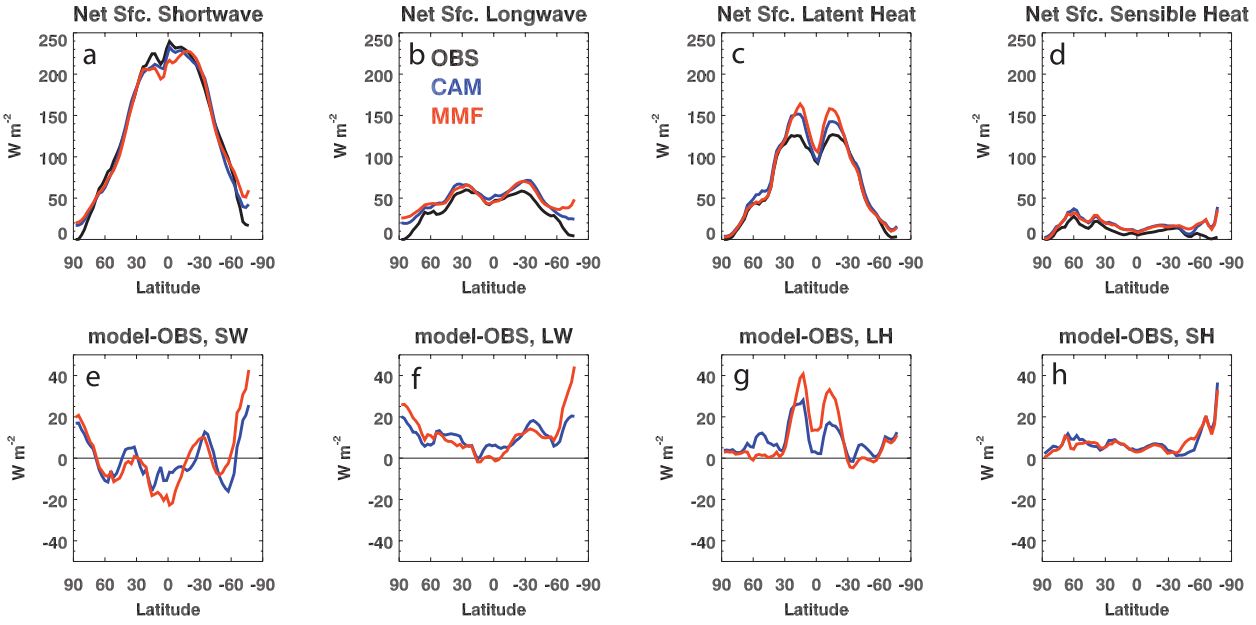

FIG. 2. (a)–(d) Zonal-mean oceanic surface fluxes (W m^{-2}). Observational estimates (black curves) are based on ISCCP data for radiation fields, OAFlux data for surface fluxes (see text). (e)–(h) Model minus observational differences.

Oceanic surface heat fluxes in Fig. 2 are presented in a familiar format (i.e., units are W m^{-2}), but they do not account for the varying ocean geometry about the globe. We present the same surface energy components in Fig. 3, this time as total energy per latitude belt [petawatts (PW)], which takes into account the varying ocean area as a function of latitude, which is the quantity integrated in the T_o calculation. Presented this way, radiation errors in the T_o calculation are seen to arise mainly from tropical shortwave and extratropical longwave biases. Large polar surface flux errors seen in Fig. 2 occur over a small area and so do not account for much of the T_o error. This presentation also emphasizes the large latent heating biases in the subtropics.

Further insight on the simulated net surface energy budget is obtained by examining the annual variability

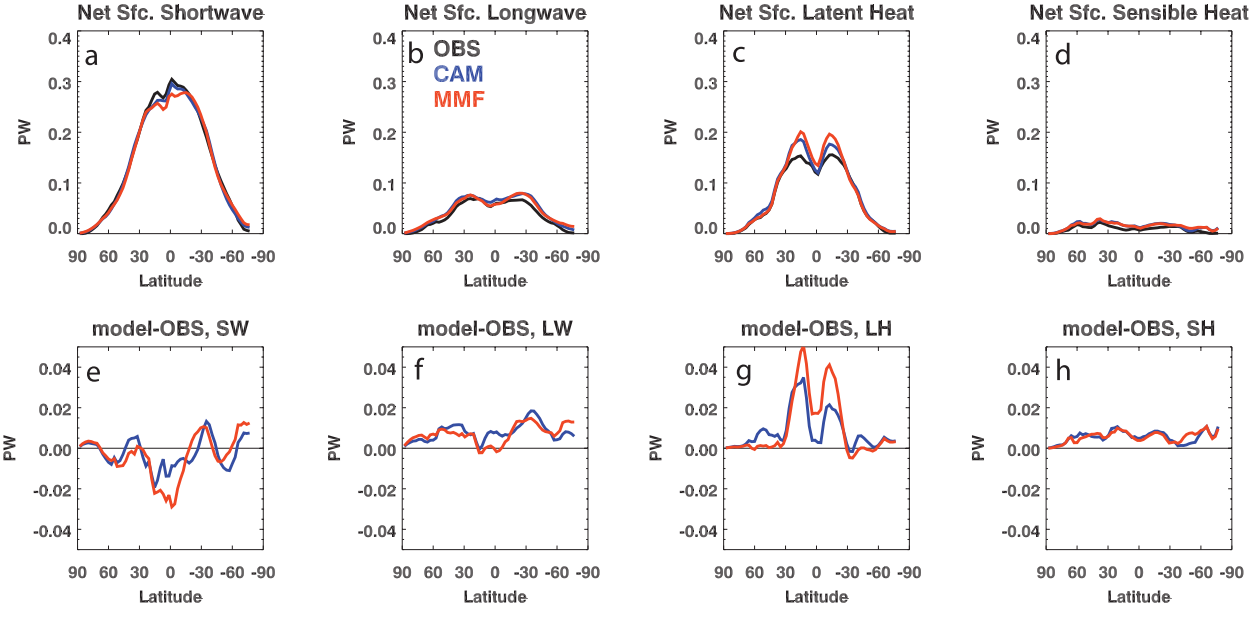

FIG. 3. As in Fig. 2, but expressed as petawatts.

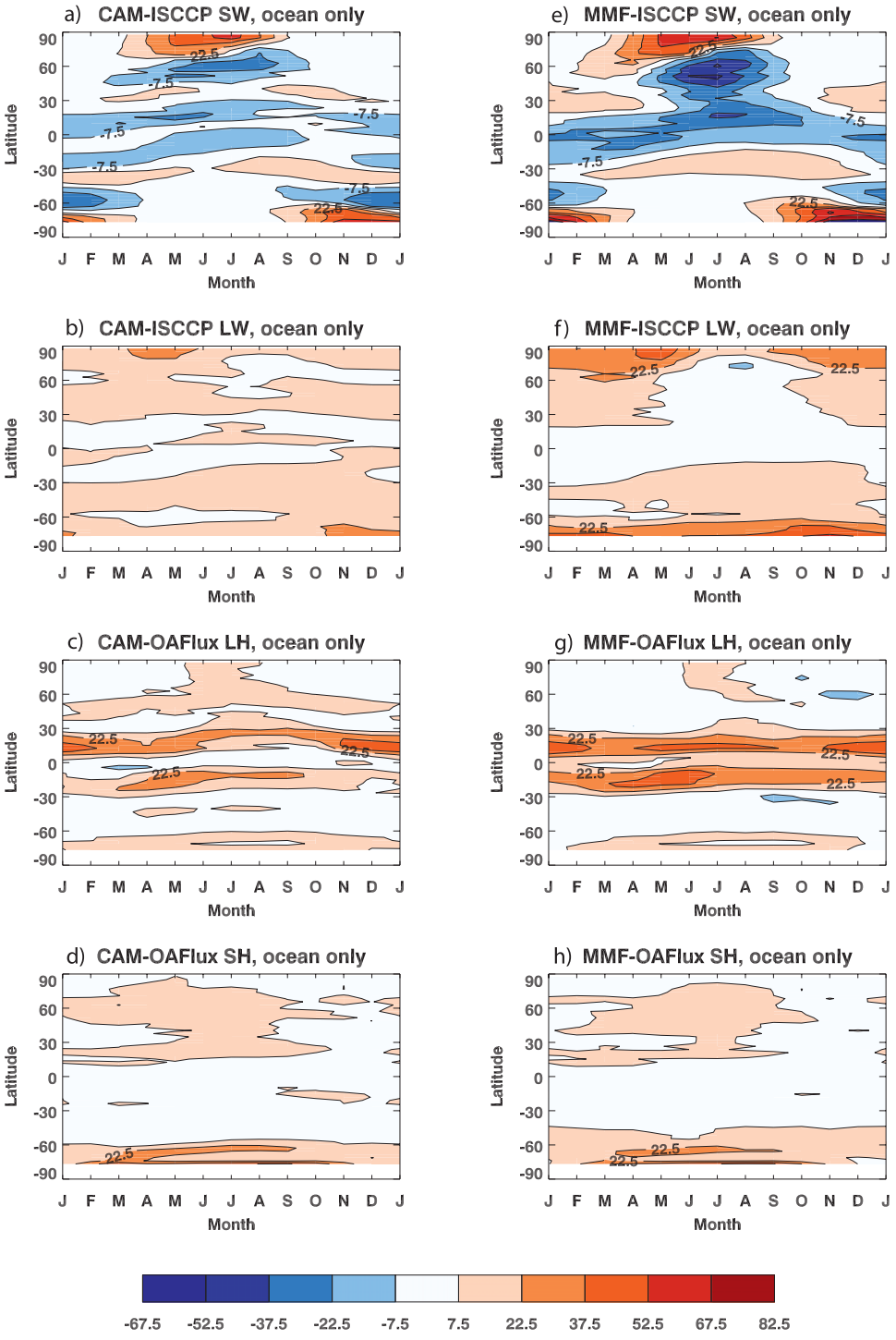

FIG. 4. Zonally averaged annual cycle of ocean-only component surface energy budget biases (W m^{-2}): SW = net surface shortwave, LW = net surface longwave, LH = latent heat flux, SH = sensible heat flux. Observational benchmark is ISCCP for radiation fields; OAFlux dataset for LH and SH fluxes.

of the component term biases, shown in Fig. 4. The shape of the annual cycle of surface SW is similar in the CAM and MMF (Figs. 4a,e), but the MMF enhances the biases present in the CAM. The MMF's large negative SW biases in the annually migrating intertropical convergence zone (ITCZ) are consistent with the notion that the MMF produces too much ice aloft in tropical convection. The greatest CAM versus MMF difference,

however, lies in June–August (JJA) Northern Hemisphere SW and is discussed in the next section. The improvement in LW heating in the MMF (Figs. 2f and 3f) results from year-round improvements in the tropics but only JJA improvements in the Northern Hemisphere midlatitudes (Figs. 4b,f).

The annual cycle of the LH fluxes reveals differences between the two models (Figs. 4c,g). In the CAM, latent heat fluxes migrate meridionally with the annual migration of the ITCZ. However, MMF LH flux biases exhibit less meridional variability, suggesting that they are strongly influenced by the stationary land–ocean contrasts. In both models, SH flux biases and their annual variability are small, and exhibit similar behaviors (Figs. 4d,h).

4. Regional and seasonal contributions to T_o

a. The T_o *error sources: Clouds and radiation*

Model bias maps for the four components of the oceanic surface heat budget are shown in Fig. 5 for JJA and Fig. 6 for December–February (DJF). CAM SW negative biases in JJA (Fig. 5a) are found primarily in the tropics and the summer hemisphere and are concentrated in the northern Indian Ocean, the northern Pacific Ocean, and offshore of the Atlantic coast of northern Africa. MMF SW negative biases in JJA (Fig. 5e) are also confined to the tropics and the summer hemisphere, but compared to the CAM they are larger in magnitude and more widespread in the Pacific and Atlantic Oceans and less prevalent in the Indian Ocean. CAM exhibits positive biases in the Maritime Continent region, and both CAM and MMF concentrate positive biases in regions of maritime stratocumulus clouds. Negative MMF SW biases, therefore, are not entirely an amplification of those found in the CAM.

We explore the causes of surface SW biases with the aid of liquid water path (LWP) and ice water path (IWP) data. Seasonal mean difference maps of simulated liquid water path (LWP) and LWP estimates from the Special Sensor Microwave Imager (SSM/I) aboard the Defense Meteorological Satellite Project (DMSP; Ferraro et al. 1996) are shown in Figs. 7a–d. Lin and Rossow (1994) detail error sources associated with passive microwave liquid water path retrievals, and Wentz (1997) and Wentz and Spencer (1998) estimate the errors to range from <1 g m^{-2} for nonprecipitating clouds to $10 \sim 15$ g m^{-2} for deep convective clouds. A negative correlation between JJA net surface SW and LWP biases for the tropics and boreal summer extratropics can be visually determined by comparing Figs. 5a and 7a for CAM, and Figs. 5e and 7c for MMF. In the tropical regions, negative SW biases are accompanied by positive LWP biases. The same is true for the North Pacific Ocean in both models. However, we note that JJA MMF SW biases in the North Pacific are much larger than those in the CAM, despite similar LWP biases in this region. For the MMF, LWP biases alone cannot explain the North Pacific SW biases, as discussed further below. The MMF also has trouble simulating surface SW in marine stratocumulus regions, where net SW is too high. The high SW biases in the Namibian, Peruvian, and Australian marine stratocumulus regions (defined in Fig. 9f) are accompanied by LWP low biases in JJA. Thus, understanding the reasons for the low bias in marine stratocumulus clouds should help improve the simulation of surface SW in these regions. This topic is discussed more below.

We next turn our attention to simulated IWP fields and their impact on surface SW. Various global IWP path retrieval techniques and their limitations are summarized in Waliser et al. (2009) and not repeated here. We have chosen CloudSat (Stephens et al. 2002) IWP estimates as the dataset for model comparison for the following reasons: 1) the active microwave sensor on CloudSat avoids the diurnal biases and saturation issues of albedo-based IWP retrievals, 2) it is sensitive to a wider range of ice particle sizes than some of the passive microwave retrieval methods, and 3) the IWP can be subdivided into precipitating and nonprecipitating components, enabling more meaningful comparisons with simulated IWP, especially for those models that instantaneously precipitate snow and graupel. Estimating errors in satellite IWP retrievals is difficult because of the scarcity of in situ global observations, but Austin et al. (2009) estimate CloudSat IWP errors to be $\pm 40\%$ relative to in situ observations. For deep convective and nimbostratus clouds, this amounts to $\pm\sim 17$ g m^{-2}, and less than $\pm\sim 5$ g m^{-2} for all other cloud types.

An important caveat to the following discussion is that IWP values based on CloudSat are considerably larger than those from other retrieval techniques (Waliser et al. 2009). We focus on tropical convection and the JJA North Pacific region, since MMF SW biases in these regions are large and have considerable impact on T_o. Annual mean IWP biases for CAM and MMF are shown in Fig. 8. To allow comparison to GCM output, Waliser et al. (2009) computed IWP values for both total and nonprecipitating cloud ice, since many GCMs, such as the CAM, do not carry precipitating ice (such as snow and graupel), but instantaneously precipitate it out of the grid column. The MMF, on the other hand, carries snow and graupel species, so IWP was computed separately for these two species and added to the nonprecipitating MMF IWP diagnostic to produce Fig. 8c. Larger (nonprecipitating) IWP in MMF compared to CAM is easily seen in Figs. 8a,b. MMF IWP biases are small compared to CloudSat IWP, but appear as positive biases compared to other retrievals. Several authors (Khairoutdinov et al. 2005, 2008; Luo

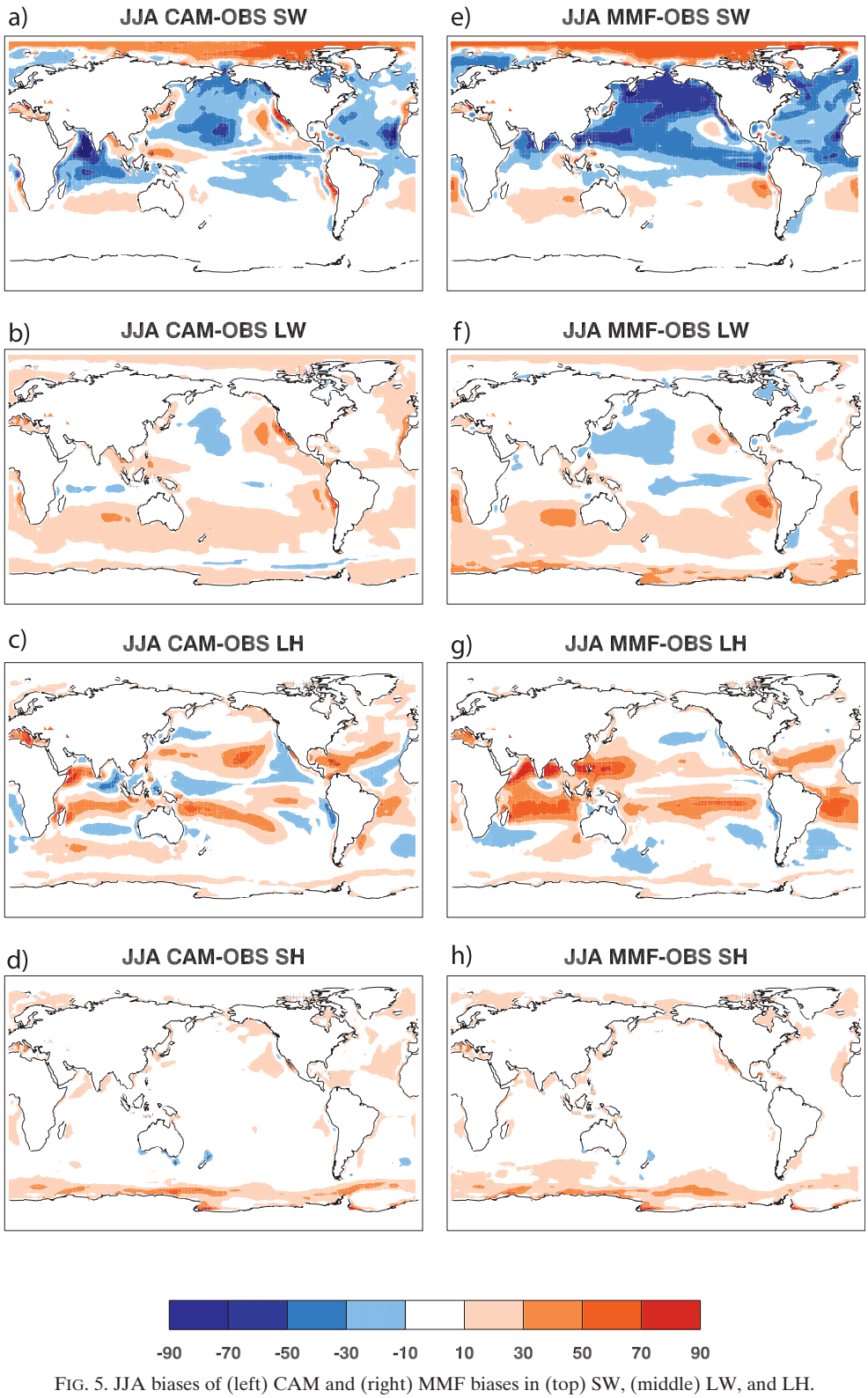

FIG. 5. JJA biases of (left) CAM and (right) MMF biases in (top) SW, (middle) LW, and LH.

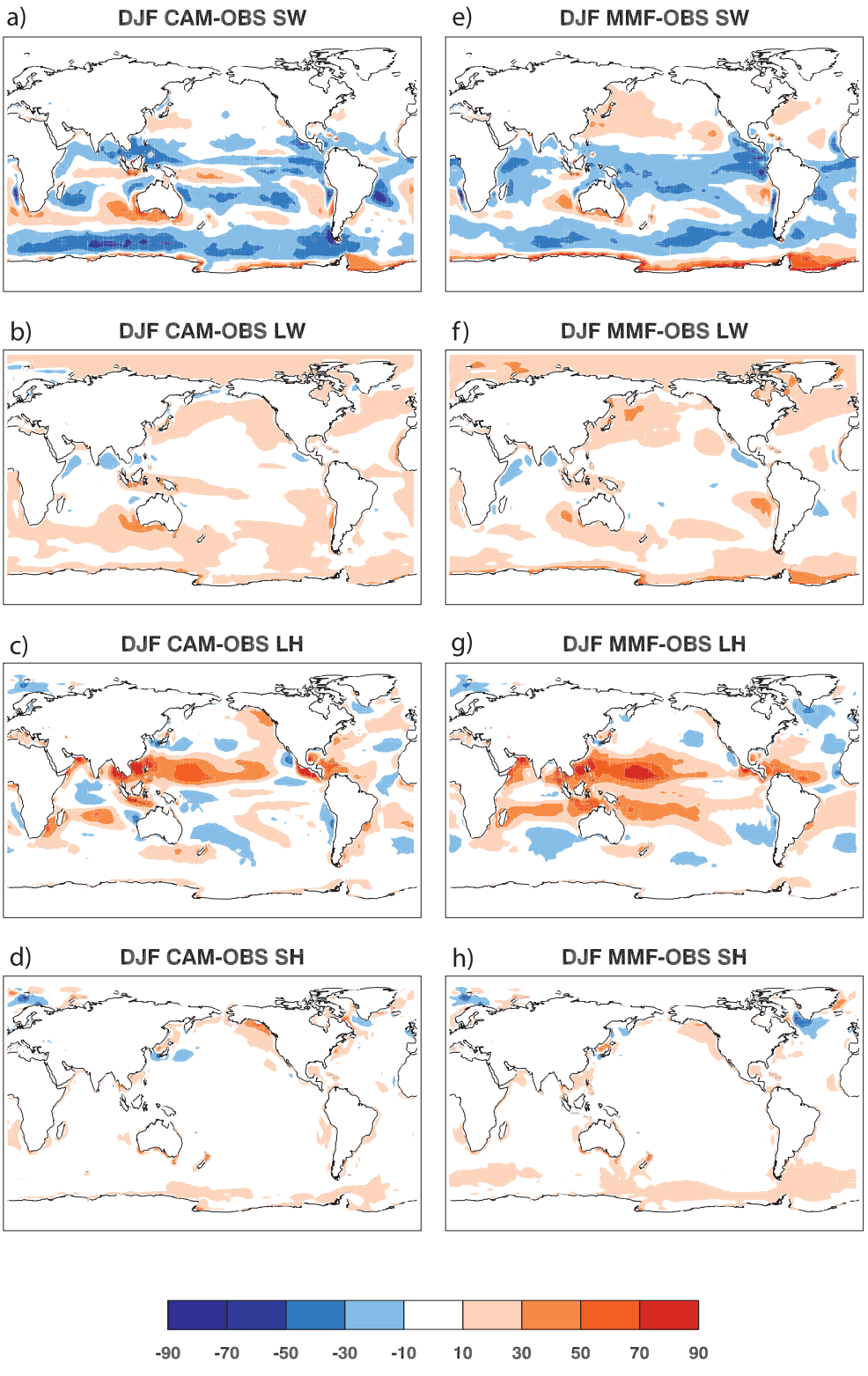

FIG. 6. As in Fig. 5, but for DJF.

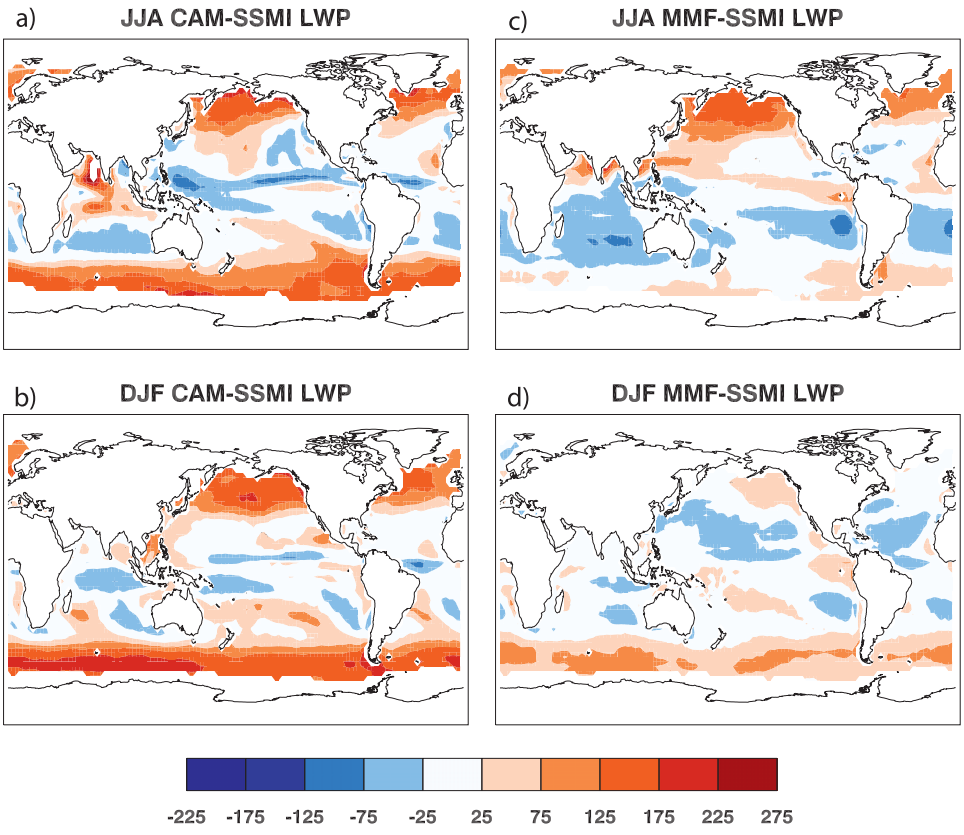

FIG. 7. Seasonal mean oceanic liquid water path biases for (left) CAM and (right) MMF. Units are 10^{-3} kg m^{-2}. SSM/I data are averaged from 1987 to 2000: (top) JJA and (bottom) DJF.

and Stephens 2006) have noted the assumed excessive tropical IWP in the MMF, which may arise from the cyclic boundary condition imposed on the cloud-resolving model embedded in the MMF. Deep convection that propagates to the edge of the CRM domain reenters the domain from the other side, and immediately encounters an environment favorable to continued convective activity that, when animated, appears to produce artificially long-lived and/or overly vigorous convection. However, if the CloudSat IWP values are believed, the conclusion is that MMF nonprecipitating IWP is correct, and the negative SW biases arise not from excessive ice water content but likely from too much small-diameter, highly reflective ice. Enhanced SW cloud forcing in the MMF compared to CAM (Khairoutdinov et al. 2005) circumstantially supports this reasoning. This could simply be the consequence of an inappropriately large ice mixing ratio threshold for the conversion of ice to snow, thereby leaving too much small ice aloft. There is little observational evidence to constrain this selection, and it is important to note that the MMF has only been minimally tuned to achieve near-zero TOA radiation balance. Further adjustments to parameters related to upper-tropospheric ice water content may be needed, and should improve the TOA radiation balance and yield more realistic ice water contents.

Similar arguments may be applied to the North Pacific in JJA, where negative cloud radiative forcing is primarily driven by large-scale stratiform cloud decks associated with transient baroclinic systems (Weaver and Ramanathan 1996). Because CAM and MMF have similar LWP biases in this region, yet the MMF SW bias is much greater than that in the CAM, the difference likely arises from cloud ice characteristics, either vertically integrated ice water content or details of the ice size distribution. CloudSat IWP retrievals support the latter explanation, while other retrieval methods would support the former.

Finally, MMF total IWP (Fig. 8c) is globally too low compared to CloudSat data. Reasons for the low bias and how it may impact surface SW are not clear, but it is possible that larger-sized ice particles are converted to precipitation too rapidly in the MMF, reducing their column density.

The MMF exhibits distinct net surface SW radiation biases in marine stratocumulus regions, which offset

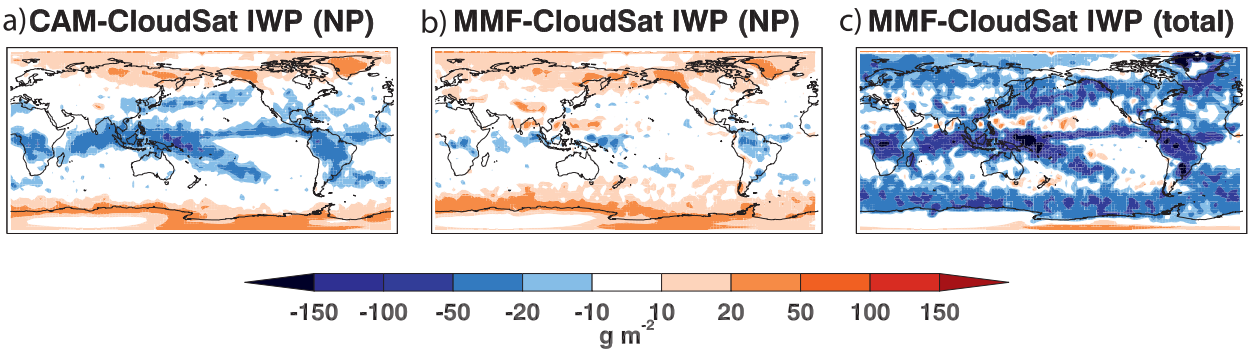

FIG. 8. Seasonal mean ice water path biases for (a) CAM and (b) MMF nonprecipitating ice as compared to August 2006–July 2007 CloudSat data nonprecipitating IWP. (c) MMF total (precipitating + nonprecipitating ice) biases compared to total IWP as determined from CloudSat. Units are 10^{-3} kg m^{-2}. CloudSat data courtesy of Duane Waliser.

some of the negative SW biases in the extratropical oceans and tropical convective regions. Such biases are either absent in the CAM (off the southern California coast in JJA, for example; Figs. 5a,e) or weaker and areally less extensive (off the west coasts of Southern Hemisphere continents in both JJA and DJF) and result from an overall lack of marine stratocumulus (Sc) clouds in the MMF (not shown). Reasons for the less-frequent occurrence of this cloud type in the MMF are not obvious. Khairoutdinov et al. (2008) demonstrated that, when present, MMF California marine Sc behaves more realistically than their CAM counterparts do. In an analysis of cloud behavior along a northeast–southwest cross section from southern California to the equatorial central Pacific, Teixeira et al. (2010, manuscript submitted to *J. Climate*) showed that the MMF produced a highly realistic along-cross-section transition from marine Sc to tropical cumulus. However, as we discuss next, MMF low-cloud fraction is not strongly correlated to lower-tropospheric stability (LTS, defined as $\theta_{\mathrm{sfc}} - \theta_{700\mathrm{mb}}$) as has been observed in nature (Klein and Hartmann 1993; Wood and Bretherton 2006), despite a reasonable representation of the annual cycle of this variable (Fig. 9).

Analysis of low-cloud behavior in relation to large-scale variables was performed for the five marine stratocumulus regions discussed in Klein and Hartmann (1993) for monthly mean values. In the CAM, low-cloud fraction is simply parameterized as a function of LTS, which is the dominant influence on marine Sc in that model. In the MMF, however, there is no parameterization for low clouds; the cloud-resolving model simply responds to the large-scale conditions and forms clouds accordingly. The relationship of LTS and low cloud in both models and observations for the regions and seasons analyzed in Klein and Hartmann (1993) is shown in Fig. 9. The close relationship between LTS and low cloud in the CAM is expected, yet is overstated for some regions (e.g., Peru) compared to the observations. MMF low clouds, which are not explicitly tied to LTS, nevertheless increase in fractional area with increasing LTS, although the affect varies greatly from region to region, and cloud fractions are much lower than those seen in either the CAM or observations.

We explored possible reasons for the low fractions of marine stratocumulus clouds by computing correlations between low-cloud fraction and several potentially relevant large-scale variables. Positive correlations between MMF low cloud and variables such as LTS, the estimated inversion strength variable of Wood and Bretherton (2006, not shown), and SST were found for some regions and some variables, but surface relative humidity (RH) and boundary layer depth were the only large-scale variables that yielded consistent relationships with MMF low-cloud fraction in all five regions. The relationship between LTS, surface RH, and low-cloud fraction for CAM, MMF, and observations is shown in Fig. 10. Both CAM and MMF exhibit similar ranges of LTS and RH on a region-by-region basis, yet MMF cloud fraction is lower than in the CAM. The broad scatter of points (for both models and observations) suggests that LTS is a poor predictor of surface RH, despite the generally positive relationship between the two.

A clearer picture emerges when cloud fraction is compared to RH and planetary boundary layer top height (PBLH) (Fig. 11). In the following discussion, it is important to note that the MMF employs no boundary layer parameterization, as subgrid-scale fluxes are computed at the CRM scale using a Smagorinski-type first-order turbulence closure (i.e., linear dependence of eddy viscosity on shear rate). MMF PBLH is diagnosed exactly as it is in the CAM, by computing the height at which the Richardson number exceeds the critical value of 0.3. PBLH is a good predictor of surface RH in the

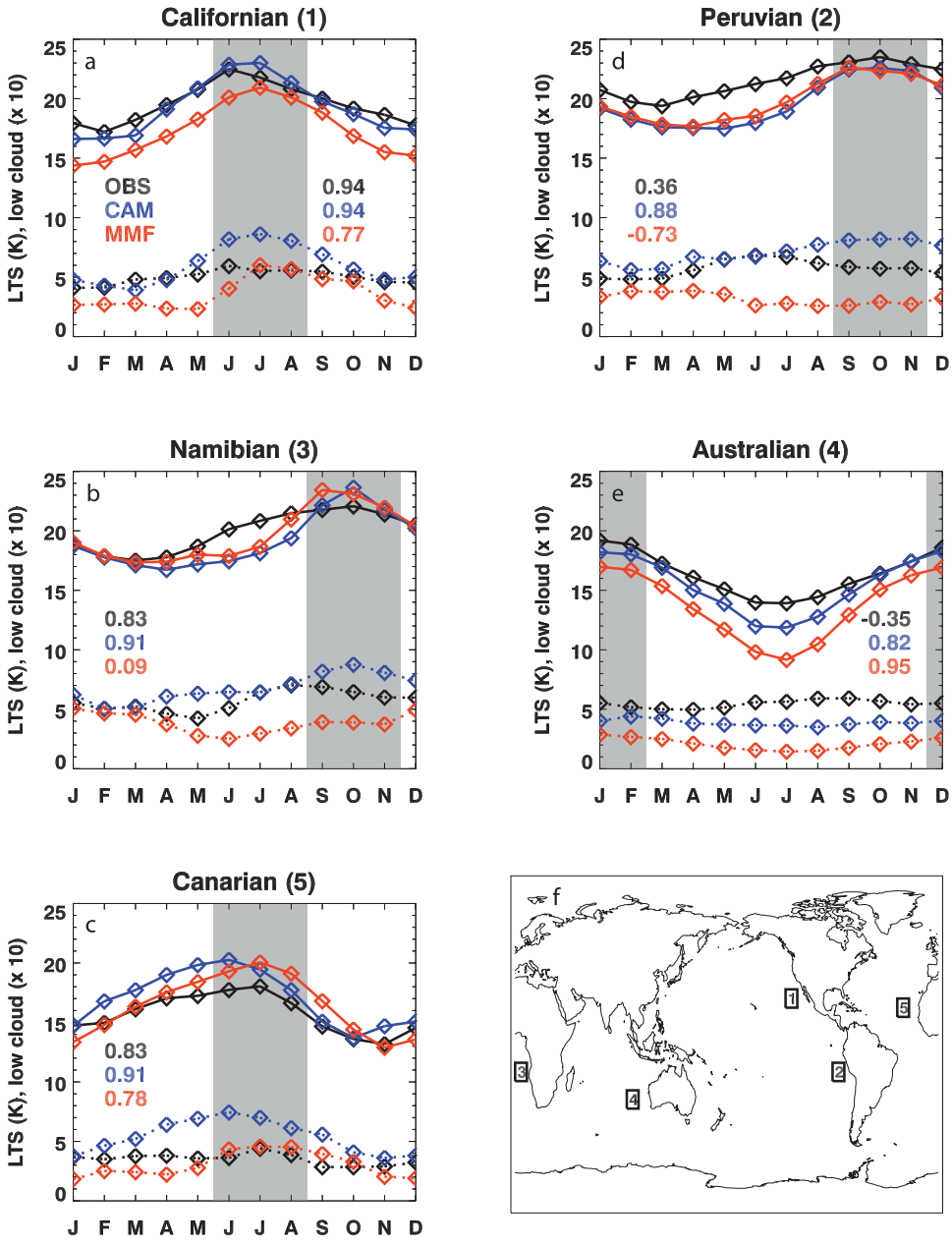

FIG. 9. (a)–(e) Mean annual cycle of LTS (solid lines) and low-cloud fraction (dashed lines, ×10) for observations (black), CAM (blue), and MMF (red) for the marine stratocumulus regions described in Klein and Hartmann (1993). (f) Low-cloud regions. Shading indicates season of maximum LTS for each region. LTS–cloud fraction annual cycle correlation is listed for each region. For observations, LTS is computed from ERA-40; low-cloud fraction is from ISCCP.

marine stratocumulus regions in each model and in observations. However, the MMF's low-cloud formation depends almost entirely on high RH values associated with shallow PBLH, whereas observed low-cloud fraction shows less sensitivity to RH. CAM low cloud is not expected to be as sensitive to RH, given its LTS-based parameterization. Figures 10 and 11 confirm that MMF low cloud generally behaves as expected based on observations (e.g., increased LTS leads to increased low cloud), but is especially sensitive to surface relative humidity.

While a positive correlation between low clouds and relative humidity in the MMF is not surprising, details of the interaction between RH, PBLH, and low cloud may

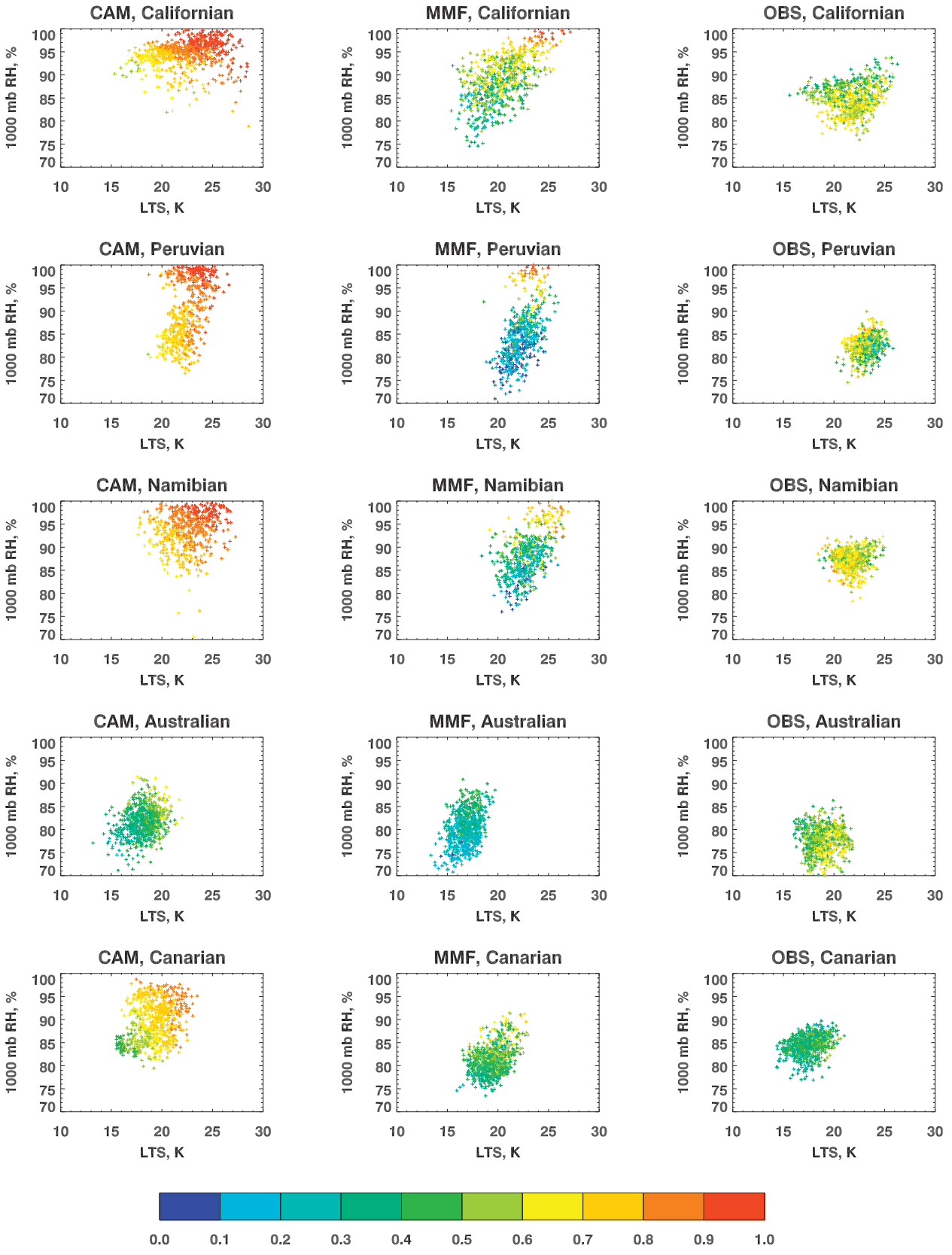

FIG. 10. Monthly mean low-level cloud fraction (ISCCP, color-coded) as a function of ERA-40 LTS and near-surface relative humidity for the five regions described in Klein and Hartmann (1993): (left) CAM, (middle) MMF, and (right) OBS.

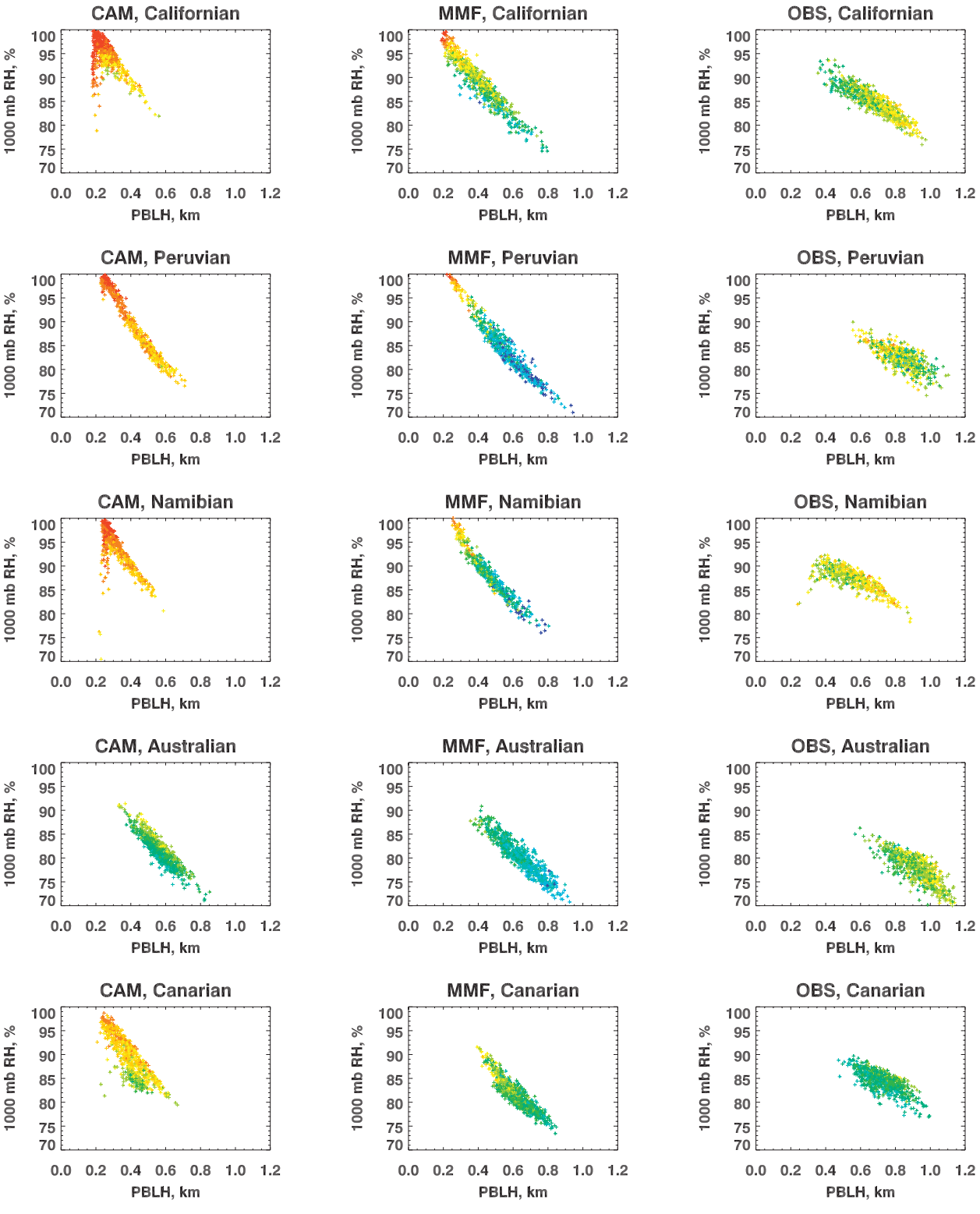

FIG. 11. As in Fig. 10, but as a function of ERA-40 boundary layer depth.

be better understood by considering the relatively coarse vertical and/or horizontal grid spacing (4 km × 4 km) of the embedded CRM. PBLH is diagnosed via the Richardson number Ri which is proportional to the ratio of buoyancy (B) to shear (S). Larger PBLH in the MMF implies a greater depth needed for Ri to exceed the critical Ri compared to the CAM. The may happen either because MMF B is too low or S is too high. The quantity B, as approximated by LTS, is similar in CAM and MMF for marine Sc regions (Fig. 10), so the difference likely arises from higher S. Greater shear in the MMF may be a consequence of the coarse grid resolution of the CRM and the Smagorinski closure assumption, producing more viscous flow (eddies as large as 4 km in horizontal scale). Physically, the larger eddies may lead to a deeper boundary layer via greater entrainment of dry atmospheric air which, for a given stability, would result in a deeper, drier boundary layer. However, the marine Sc MMF PBL RH is still greater than that seen in observations. Although Allan et al. (2004, their Fig. 2) present evidence indicating that low biases may exist in ERA-40 marine Sc water vapor estimates, MMF PBL RH could also be too high because the larger, more viscous eddies may not be as efficient at transporting moisture as smaller, less viscous eddies.

b. The T_o *error sources: Latent heat fluxes*

CAM and MMF area-weighted latent heat flux errors are primarily confined to the tropics and subtropics (Fig. 3). The annual cycle of the latent heat flux biases (Fig. 4) suggests that the biases are associated with the trade winds. However, whereas the CAM biases migrate north and south throughout the year with the progression of the ITCZ, MMF biases are essentially locked onto fixed latitudes, suggesting a greater influence of fixed landmasses in the MMF than in the CAM. This idea is further explored by presenting seasonal mean biases of latent heat flux, surface wind stress, near-surface relative humidity, and rainfall in the CAM and MMF for JJA (Fig. 12) and DJF (Fig. 13).

Positive JJA CAM latent heat flux biases (Fig. 12a) are concentrated in the subtropical oceans. With the possible exception of the positive bias off the Somali coast, the biases are not concentrated at any particular location; that is, they occur rather uniformly across the subtropics. In contrast, JJA MMF latent heat flux biases (Fig. 12e) are greater than those in the CAM, are more zonally oriented, and exhibit a broad, intense regional maximum in the Asian monsoon regions of the Indian and western Pacific Oceans.

The geographical relationship between latent heat fluxes, surface wind stress, and near-surface relative humidity is examined with the aid of Figs. 12b,f (surface stress biases) and Figs. 12c,g (RH biases). We focus our discussion on the tropical and subtropical regions. CAM positive LH biases are mimicked by positive surface stress biases and negative RH biases, especially in the Somali jet region. CAM negative LH biases have a greater tendency to be accompanied by negative surface stress and positive RH biases, such as in the Bay of Bengal, and especially in the marine stratocumulus regions. MMF JJA surface stress and RH biases reveal an unusual situation in the Somali jet–Asian monsoon–western Pacific region, where large positive surface stress biases are accompanied by positive relative humidity biases. Despite the moist surface air in this region, surface stresses are strong enough to produce excessive latent heat fluxes. As in the CAM, the largest MMF surface stress biases are anchored over the Somali jet region, yet they extend much farther east, over landmasses, and into the western Pacific Ocean. Looking beyond the Asian monsoon region to the subtropical belt as a whole, MMF negative surface RH biases are more widespread than in the CAM and are particularly pronounced in the marine stratocumulus regions, giving a geographical context to the RH–cloud fraction relation illustrated in Fig. 11.

Precipitation biases are shown in Figs. 12d,h, illustrating their spatial relation to latent heat flux, surface stress, and relative humidity biases, particularly in the tropics. CAM JJA precipitation biases are greatest in the Indian Ocean and are collocated with the positive latent heat flux biases in this region. Other major precipitation biases are also accompanied by same-signed latent heat flux biases, especially in the Pacific Ocean, and less so in the Atlantic Ocean. Positive MMF JJA precipitation biases are concentrated in the ITCZ and, dramatically, in the Asian monsoon-to-western Pacific region of anomalously high LH flux and surface stress biases.

The MMF's high precipitation bias in the western Pacific has received much attention (Khairoutdinov et al. 2005, 2008; Luo and Stephens 2006), but it appears to be the easternmost extension of a large, overly active convective region rooted over the summertime Somali jet, spreading from the Arabian Sea, to the Bay of Bengal, and into the western Pacific. This is confirmed in plots of vertically integrated meridional moisture flux (not shown) and leads to an enhanced Hadley circulation in the MMF, particularly in JJA. The additional subsidence required to balance the enhanced upward motion in the MMF is realized via fractionally larger areas of subsidence within the subtropics but does not result in any latitudinal broadening of the Hadley circulation. Tropical and subtropical subsidence in the MMF is slightly greater than that in the CAM, and closer to subsidence derived from the NCEP reanalysis, which slightly exceeds MMF subsidence.

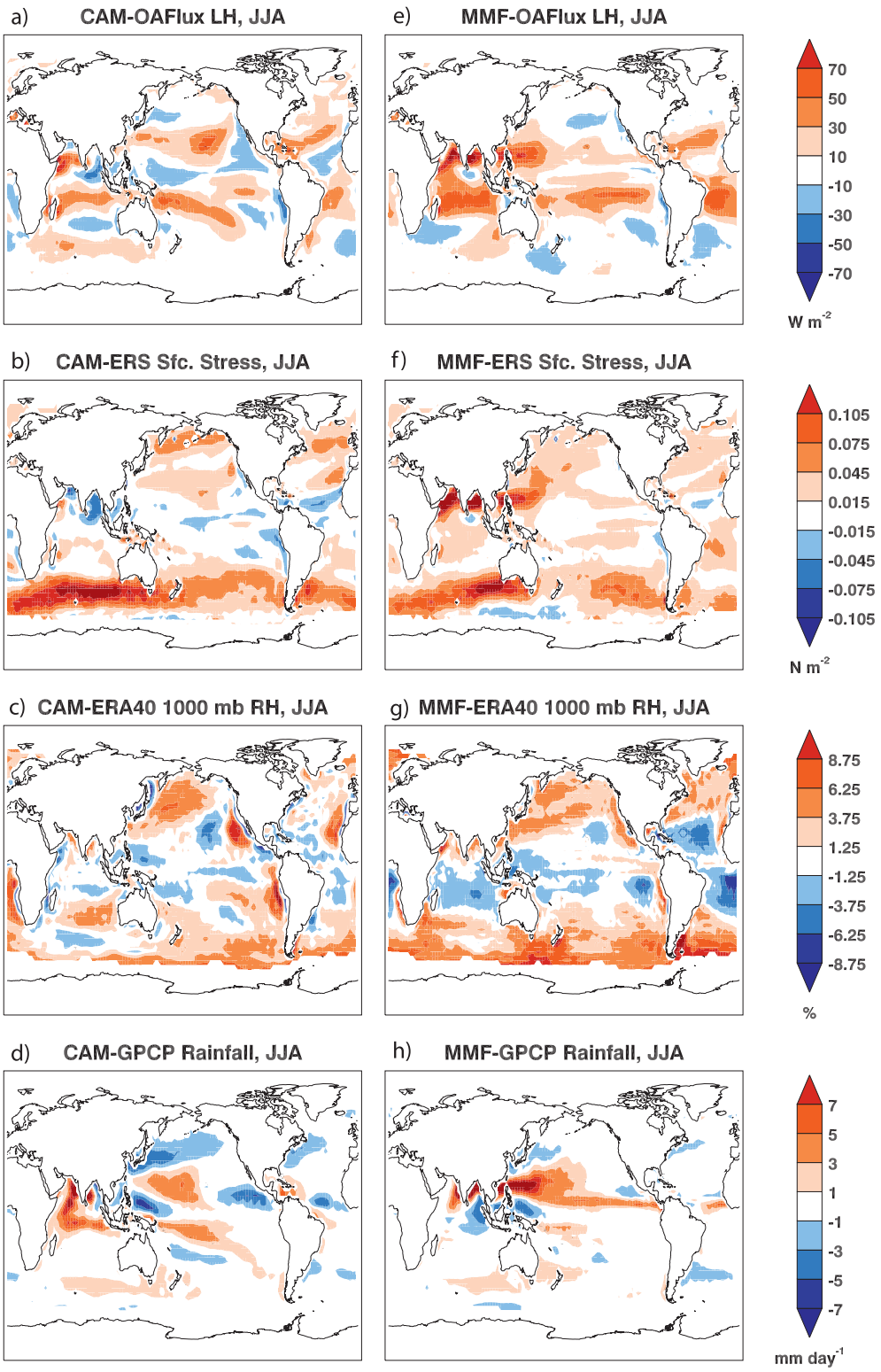

FIG. 12. Model minus observational estimates for JJA (a),(e) surface latent heat flux; (b),(f) surface stress; (c),(g) relative humidity at 1000 mb; and (d),(h) precipitation.

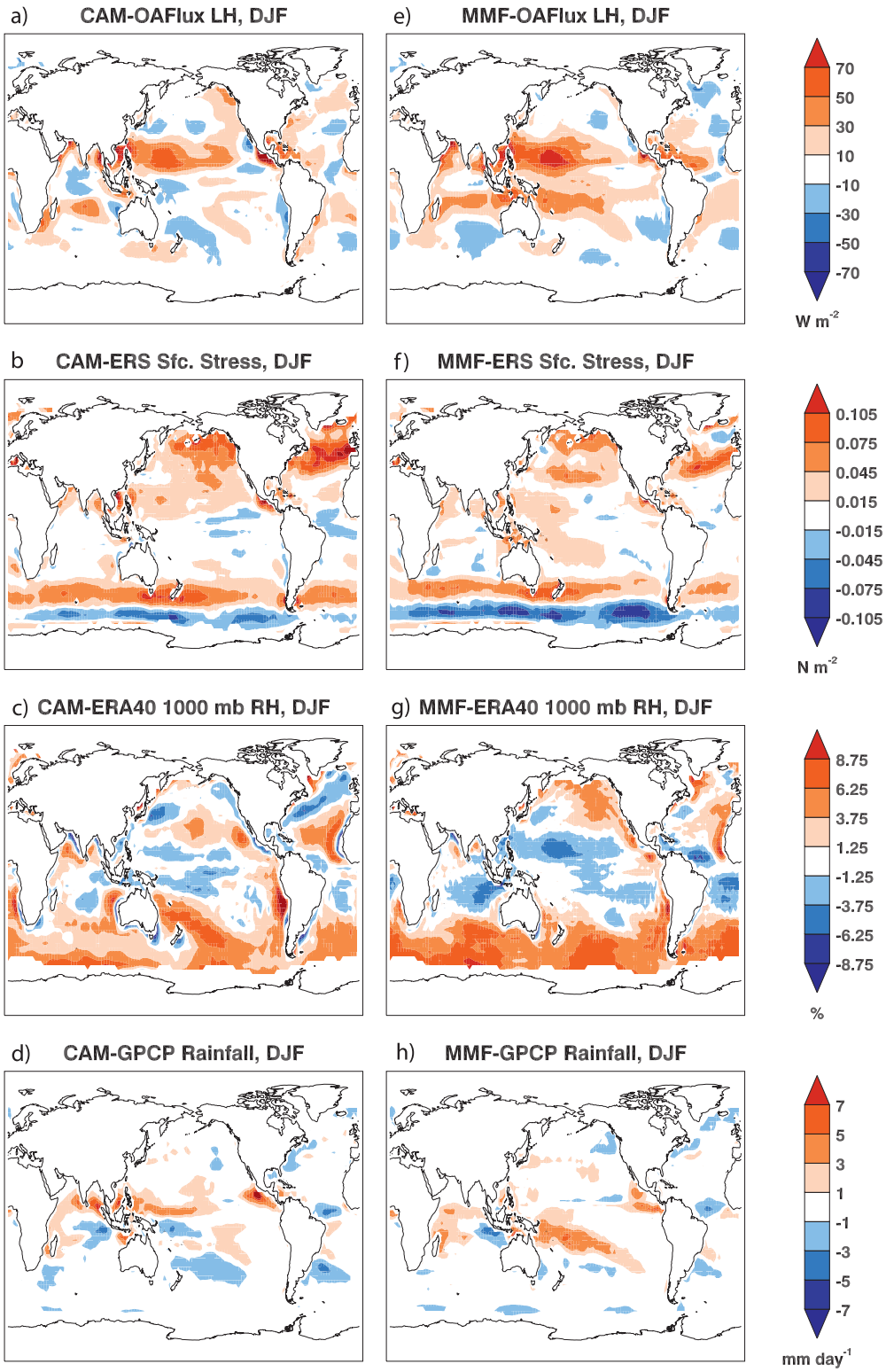

FIG. 13. As in Fig. 12, but for DJF.

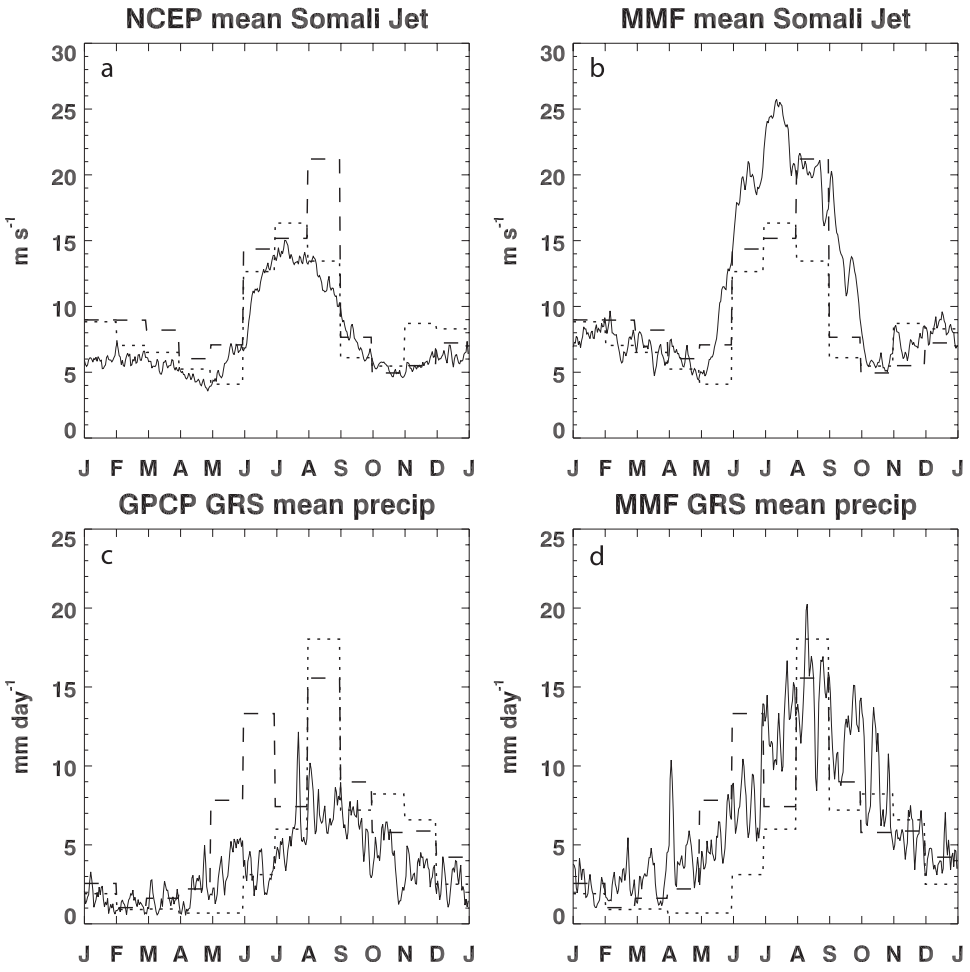

FIG. 14. Mean annual cycle of the daily Somali jet index (SJI = 850 mb wind speed) in (a) NCEP reanalysis and (b) MMF (solid curves) and (c) GPCP and (d) MMF western North Pacific (WNP; 15°–25°N, 120°–160°E) precipitation (solid curves). Solid curves are based on 7 yr worth of daily mean data. Single-year realizations of SJI and WNP precipitation from 3D CRM test runs are overlaid for comparison (dashed line = 3d CRM; dotted line = 3d CRM with convective momentum transports).

There is some evidence that Asian monsoon region precipitation biases, such as that seen in the MMF, are common to AMIP-style simulations (Wang et al. 2004), arising from the one-way interaction of ocean temperatures on the atmosphere and the absence of atmospheric effects on ocean temperatures. For example, western Pacific JJA CAM and MMF precipitation biases bear some resemblance to the JJA 1998 eleven-model ensemble precipitation bias in Fig. 10 of Wang et al. (2004), which suggests that some of the positive bias may be attributable to the noninteractive SST boundary condition. However, questions regarding the larger bias in the MMF than in the CAM remain. Maps of JJA MMF surface stress (Fig. 12f) reinforce the notion that the Somali jet is the ''anchor point'' for the large-scale precipitation bias, as the surface stress and LH bias patterns mimic that of precipitation biases in the Asian monsoon region. MMF seasonal mean precipitation anomalies in this region resemble May-to-October precipitation anomalies associated with the MJO, as presented in CLIVAR Madden–Julian Oscillation Working Group (2009; their Fig. 11) and Lin et al. (2008; their Fig. 1). However, as in the observations, there is no statistically significant correlation between the MMF's low-level Somali jet–area meridional winds and western Pacific rainfall maximum at MJO or other frequencies. It appears, therefore, that the MMF's larger-than-observed LH flux and precipitation in this region are simply exaggerations of the annual cycles of these two variables, as shown in Fig. 14.

The two-dimensional configuration of the CRM and absence of convective momentum transports may play a role in generating overly vigorous convection in this region. To investigate this possibility, output from two

developmental versions of the MMF (Khairoutdinov and Randall 2003), which utilized a limited-area three-dimensional CRM with and without convective momentum transports, were analyzed. These two model versions produced improvements in the annual cycles of the Somali jet index and western Pacific rainfall (see Fig. 14). However, global distributions of surface LH flux and surface stress (not shown) indicate that improvements in some tropical regions are offset by increased biases in other regions. These results allow only the most general of interpretations and do not address the issue of the CRM's cyclic boundary condition. They do, however, illustrate that a two-dimensional representation of convection in convectively active areas is not able to fully capture the interactions of the convective- and large-scale circulations and that a three-dimensional representation of convection may offer some improvement.

Analyses of DJF latent heat flux and related fields (see Fig. 13) reinforce many of the points described above. Positive MMF LH flux biases again show a strong tendency to be aligned to ~20°N and 20°S, but are shifted more toward the central Pacific. As expected, maxima in LH flux biases in each model are accompanied by maxima in surface stress. Aside from the Southern Hemisphere storm belt (a region that contributes little to implied ocean heat transport errors), the greatest difference in season-to-season surface stress biases is found in the Asian monsoon region of the MMF. The dominant biases of this region seen in JJA (Fig. 12f) are barely existent in DJF (Fig. 13f). In the CAM, surface RH biases generally exist with opposite-signed LH flux biases but on smaller spatial scales than the LH flux biases. The tendency for tropical and subtropical surface RH to be too low in the MMF remains in DJF and appears to play an enhanced role in the Pacific basin positive LH flux biases. Finally, CAM and MMF DJF precipitation bias magnitudes are smaller than their JJA counterparts.

5. Discussion and conclusions

The goals of our study are to assess CAM and MMF globally integrated net surface energy budget biases on implied ocean heat transports T_o and to identify specific physical processes, or at least regions or seasons where such processes are likely to occur, that contribute to errors in T_o. Compared to the observational results of Trenberth and Caron (2001), both CAM and MMF transport too much energy poleward in the Northern Hemisphere and not enough energy poleward in the Southern Hemisphere. In fact, the MMF is characterized by northward transport in much of the Southern Hemisphere. For both the CAM and MMF, the largest sources of error in T_o are net surface shortwave radiation and latent heat fluxes. SW errors in the MMF are greater than those in the CAM and are concentrated in the tropics. MMF ice water content profiles and outgoing longwave radiation maps (Khairoutdinov et al. 2005) suggest the need for further tuning of convective ice water processes, which should produce more realistic cloud structures and SW radiation fields in tropical regions characterized by deep convection.

MMF surface SW radiation biases associated with marine stratocumulus clouds present a more challenging problem. Khairoutdinov et al. (2008) demonstrated that the MMF produces realistic, but too infrequent, marine stratocumulus clouds. MMF marine low clouds are highly sensitive to low-level relative humidity, which is in turn largely controlled by boundary layer depth in that model. Seasonal mean maps of low-level relative humidity (Figs. 12 and 13) confirm that the MMF low-level relative humidity is too low over much of the ocean surface. The potential feedbacks between the embedded CRM and the large-scale GCM on low-level humidity are difficult to determine from our analyses and point to the need for further study.

Positive latent heat flux biases in the MMF are predominantly located in the tropics and trade wind regimes, with the largest biases located in regions characterized by frequent, deep convection. Unlike the smaller-magnitude CAM biases, MMF LH flux biases show little poleward migration throughout the annual cycle, suggesting an enhanced sensitivity to land–ocean configurations. MMF positive LH fluxes are generally collocated with a broad region of anomalously high relative humidity and rainfall in the Asian monsoon region. LH and precipitation anomalies in this region show no preferred periodicity other than an overenhancement of the observed mean annual cycle. The model formulation of the MMF's embedded cloud-resolving model, with its two-dimensional structure and cyclic boundary condition, may contribute to the enhanced convective activity (Khairoutdinov et al. 2005).

The final point to address is how anticipated improvements in the MMF's surface radiation and latent heat budgets may improve its implied oceanic heat transport. We evaluate this by replacing the simulated net surface shortwave radiation with that from ISCCP, or the simulated latent heat fluxes with those from the OAFlux dataset, and recompute the implied ocean transports for both models. The results, shown in Fig. 15, include the area-weighted rms error in net surface energy budget for each simulation. When simulated SW fluxes are replaced with ISCCP SW fluxes, T_o improves for both CAM and MMF. The rms errors decrease for both models, although more improvement is seen in the MMF. The improvement in MMF T_o is encouraging,

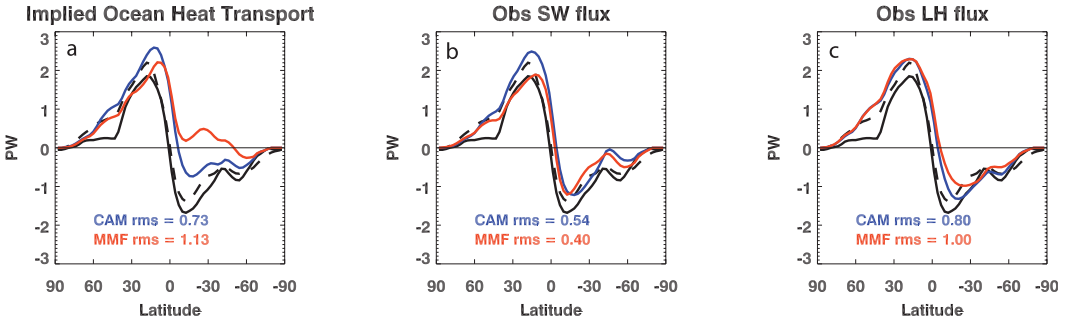

FIG. 15. Implied ocean heat transport curves for CAM (blue) and MMF (red) (a) as computed from model output, (b) with ISCCP net surface SW fluxes in place of model net surface SW fluxes, and (c) with OAFlux LH estimates in place of model LH fluxes. NCEP (solid black), and ERA-40 (dashed black). Model − observation rms differences in the total net surface energy budget are shown for each calculation.

since the primary improvements needed to achieve better net surface SW fluxes are related to ice microphysics, which may be affected simply by adjusting ice-to-snow conversion parameters or, more elegantly, by the planned introduction of a two-moment ice microphysical scheme to the cloud-resolving model. Replacing simulated LH fluxes with the OAFlux estimates results in a less-dramatic improvement in MMF T_o, but corrects the unrealistic northward transport in the Southern Hemisphere. Changes in the CAM net surface energy budget are less than 10%.

Our analysis has examined sources of error in the surface energy budgets of the CAM and MMF under AMIP-type conditions. Some errors are rooted in the treatment of atmospheric processes (such as marine stratocumulus clouds and ice microphysics), but some may be linked to the one-way interaction of ocean SSTs on the atmosphere (monsoon region convective intensity, for example). The results point to areas of needed model improvement in the MMF and pique our curiosity concerning the utility of the MMF for atmosphere–ocean coupled simulations.

Acknowledgments. This work was supported by the National Science Foundation Science and Technology Center for Multi-Scale Modeling of Atmospheric Processes, managed by Colorado State University under Cooperative Agreement ATM-0425247. Additional funding was provided by DOE ARM Grant DE-FG02-02ER63370 and DOE SciDAC Contract DE-FC02-06ER64302. Observational datasets were obtained from the following sources: ISCCP online data source (http://isccp.giss.nasa.gov/products/isccpDsets.html), ECMWF (http://www.ecmwf.int/research/era/do/get/era-40), ISCCP Monthly Means (http://www.cgd.ucar.edu/cas/catalog/satellite/isccp/D2/means.html), NCEP–NCAR reanalysis project at the NOAA/ESRL Physical Sciences Division (http://www.cdc.noaa.gov/cdc/reanalysis/reanalysis.shtml), OAFLux for the Global Oceans (http://oaflux.whoi.edu/index.html), and Earthnet Online (http://earth.esa.int/ers/). CloudSat ice water path data were kindly provided by Frank Li and Duane Waliser of NASA Jet Propulsion Laboratory. We thank William Rossow and Kevin Trenberth for helpful discussions concerning this analysis.

REFERENCES

Allan, R. P., M. A. Ringer, J. A. Pamment, and A. Slingo, 2004: Simulation of the earth's radiation budget by the European Centre for Medium-Range Water Forecasts 40-year reanalysis (ERA40). *J. Geophys. Res.,* **109,** D18107, doi:10.1029/2004JD004816.

Austin, R. T., A. J. Heymsfield, and G. L. Stephens, 2009: Retrieval of ice cloud microphysical parameters using the CloudSat millimeter-wave radar and temperature. *J. Geophys. Res.,* **114,** D00A23, doi:10.1029/2008JD010049.

Barkstrom, B. R., and J. B. Hall Jr., 1982: Earth Radiation Budget Experiment (ERBE): An overview. *J. Energy,* **6,** 141–146.

Bryan, K., 1962: Measurements of meridional heat transport by ocean currents. *J. Geophys. Res.,* **67,** 3403–3414.

Carissimo, B. C., A. H. Oort, and T. H. Vonder Haar, 1985: Estimating the meridional energy transports in the atmosphere and ocean. *J. Phys. Oceanogr.,* **15,** 82–91.

CLIVAR Madden–Julian Oscillation Working Group, 2009: MJO simulation diagnostics. *J. Climate,* **22,** 3006–3030.

Collins, W. D., and Coauthors, 2006: The formulation and atmospheric simulation of the Community Atmosphere Model Version 3 (CAM3). *J. Climate,* **19,** 2144–2161.

DeMott, C. A., D. A. Randall, and M. Khairoutdinov, 2007: Convective precipitation variability as a tool for general circulation model analysis. *J. Climate,* **20,** 91–112.

Ferraro, R. R., F. Weng, N. C. Grody, and A. Basist, 1996: An eight-year (1987–1994) time series of rainfall, clouds, water vapor, snow cover, and sea ice derived from SSM/I measurements. *Bull. Amer. Meteor. Soc.,* **77,** 891–905.

Gates, W. L., 1992: AMIP: The Atmospheric Model Intercomparison Project. *Bull. Amer. Meteor. Soc.,* **73,** 1962–1970.

Gleckler, P. J., and Coauthors, 1995: Cloud-radiative effects on implied oceanic energy transports as simulated by atmospheric general circulation models. *Geophys. Res. Lett.,* **22,** 791–794.

Hack, J. J., 1998: Analysis of the improvement in implied meridional ocean energy transport as simulated by the NCAR CCM3. *J. Climate,* **11,** 1237–1244.

——, B. A. Boville, B. P. Briegleb, J. T. Kiehl, P. J. Rasch, and D. L. Williamson, 1993: Description of the NCAR Community Climate Model (CCM2). Tech. Rep. NCAR/TN-382+STR, National Center for Atmospheric Research, 120 pp.

Hasternath, S., 1980: Heat budget of tropical ocean and atmosphere. *J. Phys. Oceanogr.,* **10,** 159–170.

Houghton, H. G., 1954: On the annual heat balance of the Northern Hemisphere. *J. Meteor.,* **11,** 1–9.

Jung, G. H., 1952: On the meridional transport of energy by the oceans. *J. Mar. Res.,* **11,** 139–146.

Khairoutdinov, M. F., and D. A. Randall, 2001: A cloud resolving model as a cloud parameterization in the NCAR Community Climate System Model: Preliminary results. *Geophys. Res. Lett.,* **28,** 3617–3620.

——, and ——, 2003: Cloud resolving modeling of the ARM summer 1997 IOP: Model formulation, results, uncertainties, and sensitivities. *J. Atmos. Sci.,* **60,** 607–625.

——, ——, and C. A. DeMott, 2005: Simulations of the atmospheric general circulation using a cloud-resolving model as a superparameterization of physical processes. *J. Atmos. Sci.,* **62,** 2136–2154.

——, C. A. DeMott, and D. A. Randall, 2008: Evaluation of the simulated interannual and subseasonal variability in an AMIP-style simulation using the CSU Multiscale Modeling Framework. *J. Climate,* **21,** 413–431.

Kistler, R., and Coauthors, 2001: The NCEP–NCAR 50-Year Reanalysis: Monthly means CD-ROM and documentation. *Bull. Amer. Meteor. Soc.,* **82,** 247–267.

Klein, S. A., and D. L. Hartmann, 1993: The seasonal cycle of low stratiform clouds. *J. Climate,* **6,** 1587–1606.

Lin, B., and W. B. Rossow, 1994: Observations of cloud liquid water path over oceans: Optical and microwave remote sensing methods. *J. Geophys. Res.,* **99** (D10), 20 907–20 927.

Lin, J.-L., K. M. Weickman, G. N. Kiladis, B. E. Mapes, S. D. Schubert, M. J. Suarez, J. T. Bachmeister, and M.-I. Lee, 2008: Subseasonal variability associated with Asian summer monsoon simulated by 14 IPCC AR4 coupled GCMs. *J. Climate,* **21,** 4541–4567.

Luo, Z., and G. L. Stephens, 2006: An enhanced convection–wind–evaporation feedback in a superparameterization GCM (SP-GCM) depiction of the Asian summer monsoon. *Geophys. Res. Lett.,* **33,** L06707, doi:10.1029/2005GL025060.

Oort, A. H., 1971: The observed annual cycle in the meridional transport of atmospheric energy. *J. Atmos. Sci.,* **28,** 325–339.

Reynolds, R. W., T. M. Smith, C. Liu, D. B. Chelton, K. S. Casey, and M. G. Schlax, 2007: Daily high-resolution blended analyses for sea surface temperature. *J. Climate,* **20,** 5473–5496.

Stephens, G. L., and Coauthors, 2002: The CloudSat mission and the A-train. *Bull. Amer. Meteor. Soc.,* **83,** 1771–1790.

Sverdrup, H. U., 1957: Oceanography. *Handbuch der Physik,* Vol. 48, Akademie-Verlag, 608–670.

Trenberth, K. E., 1979: Mean annual poleward energy transports by the oceans in the Southern Hemisphere. *Dyn. Atmos. Oceans,* **4,** 57–64.

——, and J. M. Caron, 2001: Estimates of meridional atmosphere and ocean heat transports. *J. Climate,* **14,** 3433–3443.

——, and J. T. Fasullo, 2008: An observational estimate of inferred ocean energy divergence. *J. Phys. Oceanogr.,* **38,** 984–999.

——, J. M. Caron, and D. P. Stepaniak, 2001: The atmospheric energy budget and implications for surface fluxes and ocean heat transports. *Climate Dyn.,* **17,** 259–276.

Uppala, S. M., and Coauthors, 2005: The ERA-40 Re-Analysis. *Quart. J. Roy. Meteor. Soc.,* **131,** 2961–3012.

Vonder Haar, T. H., and A. H. Oort, 1973: New estimate of annual poleward energy transport by Northern Hemisphere oceans. *J. Phys. Oceanogr.,* **3,** 169–172.

Waliser, D. E., and Coauthors, 2009: Cloud ice: A climate model challenge with signs and expectations of progress. *J. Geophys. Res.,* **114,** D00A21, doi:10.1029/2008JD010015.

Wang, B., I.-S. Kang, and J.-Y. Lee, 2004: Ensemble simulations of Asian–Australian monsoon variability by 11 AGCMs. *J. Climate,* **17,** 803–818.

Weaver, C. P., and V. Ramanathan, 1996: The link between summertime cloud radiative forcing and extratropical cyclones in the North Pacific. *J. Climate,* **9,** 2093–2109.

Wentz, F. J., 1997: A well-calibrated ocean algorithm for SSM/I. *J. Geophys. Res.,* **102,** 8703–8718.

——, and R. W. Spencer, 1998: SSM/I rain retrievals within a unified all-weather ocean algorithm. *J. Atmos. Sci.,* **55,** 1613–1627.

Williamson, D. L., and J. G. Olson, 1994: Climate simulations with a semi-Lagrangian version of the NCAR Community Climate Model. *Mon. Wea. Rev.,* **122,** 1594–1610.

Wood, R., and C. S. Bretherton, 2006: On the relationship between stratiform low cloud cover and lower-tropospheric stability. *J. Climate,* **19,** 6425–6432.

Xie, P., and P. A. Arkin, 1997: Global precipitation: A 17-year monthly analysis based on gauge observations, satellite estimates, and numerical model outputs. *Bull. Amer. Meteor. Soc.,* **78,** 2539–2558.

Yu, L., and R. A. Weller, 2007: Objectively analyzed air–sea heat fluxes for the global ice-free oceans (1981–2005). *Bull. Amer. Meteor. Soc.,* **88,** 527–539.

Zhang, G. J., and N. A. McFarlane, 1995: Sensitivity of climate simulations to the parameterization of cumulus convection in the Canadian Climate Centre general circulation model. *Atmos.–Ocean,* **33,** 407–446.

Zhang, Y., W. B. Rossow, A. A. Lacis, V. Oinas, and M. I. Mishchenko, 2004: Calculation of radiative fluxes from the surface to top of atmosphere based on ISCCP and other global data sets: Refinements of the radiative transfer model and the input data. *J. Geophys. Res.,* **109,** D19105, doi:10.1029/2003JD004457.